Table 4 Multivariate analysis of prognostic factors for overall survival

Prognostic factors	Risk ratio	(95% confidence interval)	*p*
Clinical stage at post-PET evaluation			
UICC, 6th edition, stage IV	0.335	(0.094–0.959)	0.041[a]
Milan criteria at post-PET evaluation			
Fulfilled	0.001	(–0.891)	0.033[a]
Child-Pugh classification at PET study			
B or C	0.482	(0.136–0.482)	0.218
Pathological grade of hepatitis			
Moderate or high	1.155	(0.159–9.122)	0.887
Post-therapeutic tumour markers			
αFP (ng/ml)=400	0.277	(0.089–0.680)	0.004[a]
Triple plus (αFP=400 & αFP-L3=15 & PIVKA-II=400)	3.964	(0.869–25.039)	0.077
Post-therapeutic FDG PET			
Visual PET diagnosis: positive	0.212	(0.042–0.661)	0.0056[a]
SUV=5	0.889	(0.337–2.451)	0.810

[a] Significant in Cox proportional hazards model

consisted of patients who were diagnosed as positive in pre- and post-therapeutic PET studies (n=10); low-high group (L-H group) which consisted of patients who were diagnosed as negative before the treatment and then showed positive uptake in the post-therapeutic PET study (n=8) (Fig. 2); and high-low group (H-L group) which consisted of patients who were diagnosed as positive before the treatment and then showed negative uptake in the post-therapeutic PET study (n=8) (Fig. 3). Figure 1b shows the survival curve of these four groups. The H-L group showed the highest survival rate in these four groups and all of them (n=8) still survived in the follow-up period. The H-H group showed the lowest survival curve. There was no difference in survival between the L-L group and L-H group. The log-rank test showed a significant different between these groups.

Discussion

FDG PET is considered as a well-established non-invasive diagnostic tool for the detection of malignant tumours [26, 27], staging and monitoring of chemotherapeutic response [28, 29] in several cancers. Shiomi et al. reported that FDG PET is useful not only for the evaluation of the malignancy but also for the prediction of outcome in patients with HCC [15]. For HCC, however, several investigators have reported that the sensitivity of FDG PET is low in the detection of HCC [17–19]. Relatively low FDG accumulation in HCC can be explained by the activity of enzymes involved in glucose metabolism. The activity of glucose-6-phosphatase (G-6-Pase), which converts FDG-6-P to FDG, is reported to be high in normal liver and nearly zero in the vast majority of tumours, including metastatic liver tumours [14, 30]. In contrast, the enzyme activity has been reported to vary widely in individual HCC; well-differentiated HCC cells exhibit an FDG metabolism similar to that of normal liver tissue, whereas undifferentiated HCC cells do not [21]. Therefore, well-differentiated HCC tends to accumulate similar amounts of FDG as normal liver, which results in relatively lower SUV. However, this enzymatic theory for FDG uptake can only be applicable in pre-operative, non-treated HCCs. As an imaging modality for the early evaluation of treatment response after non-operative therapy for HCC, the role of FDG PET has not been established, nor reported so far.

Interventional therapy, such as TACE or TAI, is considered to be an effective palliative treatment in patients with HCC [31, 32]. However, a meta-analysis of randomized clinical trials showed that a survival advantage associated with therapeutic chemoembolization versus supportive care alone has not been clearly proven so far [33]. Therefore, it is clinically important to analyse the therapeutic effect of non-operative therapy as soon as possible, because inefficacious palliative treatment may be not only useless but also harmful for patients with advanced HCC. Conventional imaging modalities, such as CT or MRI, cannot satisfy clinicians in that context, because therapy evaluation by these anatomical imaging modalities requires sufficient time to confirm tumour shrinkage [34, 35]. Herein, PET, as a metabolic imaging modality, is expected to be useful in electing to proceed or terminate therapy. Our data in the present study showed that FDG PET could evaluate therapeutic effect and prognostic value in patients with unresectable HCC. To our knowledge, the present study is the first report evaluating the effectiveness of FDG PET in the early therapeutic response evaluation in unresectable HCC patients treated by non-operative therapies.

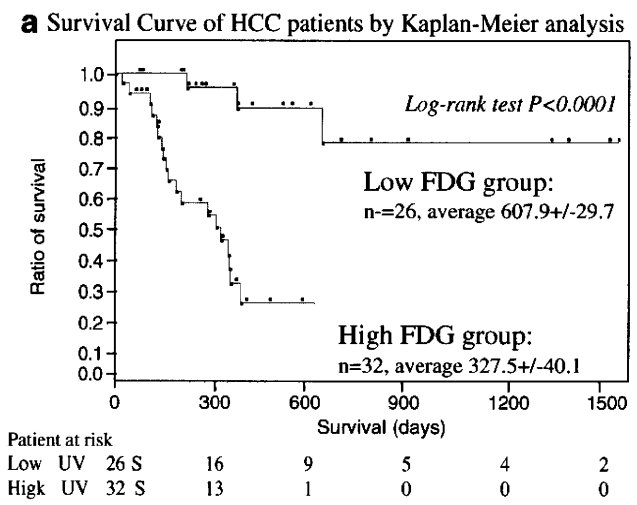

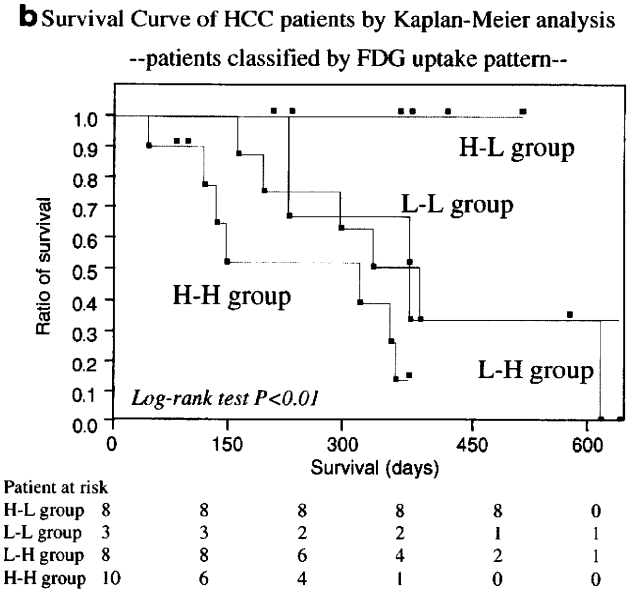

Fig. 1 Survival curve of HCC patients by Kaplan-Meier analysis. **a** The overall survival rate in HCC patients treated by non-operative therapy was significantly higher in the low FDG group than that in the high FDG group ($p<0.0001$). **b** The overall survival rate in four groups of patients classified by the FDG uptake pattern (see exact definition in the text) is shown. The H-H group showed poor survival. On the other hand, the H-L group showed the best survival with 100% survival rate in the follow-up period. There was no difference between the L-H group and L-L group. The log-rank test showed that there was a significant difference between the four groups ($p<0.01$)

Our principal finding is that visual FDG PET diagnosis after non-operative therapy is an independent predictor of survival in unresectable HCC patients. This is compatible with a variety of previous studies performed in other malignancies [36–38]. Table 2 also clearly reveals the advantage of FDG PET diagnosis in early post-therapeutic evaluation with respect to the prediction of patient survival. High negative predictive value (94.4%) means that patients with negative post-therapeutic PET result are supposed to survive at least 12 months, while high positive predictive value (100%) means that patients with positive post-therapeutic PET result are supposed to die within 24 months. We believe that post-therapeutic FDG PET after non-operative therapy would make a great contribution in the clinical management of patients with unresectable HCCs, such as in electing to proceed or terminate therapy, altering the chemotherapeutic regimen, choosing treatment modalities or in other decisions.

On the other hand, FDG PET within 1 month after non-operative therapy is not sensitive in the diagnosis of lesion viability. Table 2 shows the limitation of FDG PET diagnosis in early post-therapeutic evaluation of HCC. Relatively low sensitivity (62.8%) and low negative predictive value (59%) in the analysis of viability of hepatic lesions suggest that negative FDG PET findings cannot ensure the complete remission of HCC after therapy. At the current moment, it is not clear what the cellular or tissue condition of the tumour is when FDG PET is negative after the non-operative therapy. It is implied, however, that they lie dormant with temporary enzymatic or other dysfunction, but can survive.

Our result shown in Fig. 2 suggests that even if FDG uptake shows a partial reduction after non-operative treatment, as observed in the H-H group, HCCs with constant positive PET finding tend to have more aggressive malignant potential. Long survival may not be expected, and continued treatment or a newly introduced therapeutic procedure would be required. On the contrary, the result of the H-L group suggests that prognostic improvement can be expected when FDG uptake disappeared. These observations provide helpful information for the management of patients with unresectable HCCs.

Bibliographically, a number of reports have been published as for the prognostic factors in patients with HCC treated by surgical procedures. Imamura et al. showed that non-anatomical resection, presence of microscopic vascular invasion and serum αFP were significant risk factors contributing to early recurrence of HCC after hepatectomy [10]. Miyaaki et al. also showed that αFP-L3 and PIVKA-II levels are potential indicators of a poor prognosis in surgically resected HCC [39]. For patients treated with liver transplantation, presence of capsule, αFP levels and viral cirrhosis were independent factors for survival [40]. Above all, the Milan criteria (single tumour: 5 cm or less in size; or three or less tumours: each 3 cm or less in size; and no macrovascular invasion) are known for their excellent outcome in the prediction of survival in patients treated with liver transplantation [24]. All these data in patients treated by surgical procedures seem to be consistent with our results. In the present study, multivariate analysis revealed that the post-therapeutic tumor marker αFP, clinical staging and Milan criteria at post-PET and visual PET diagnosis are significant prognostic factors (Table 4). This is also basically compatible (except for PET diagnosis) with the previous report using multivariate analysis

Table 5 Comparison of high FDG and low FDG groups

	High FDG group (n=32)	Low FDG group (n=26)	p
Age (years)			
Mean±SD	59.5±13.3	62.4±10.4	n.s.
Range	34–80	42–78	
Gender, n (%)			
Male	26 (81)	20 (77)	n.s.
Female	6 (19)	6 (23)	
Tumour differentiation, n (%)			
Well	2 (6)	1 (4)	n.s.
Moderately	10 (31)	6 (23)	
Poorly	8 (25)	6 (23)	
Unknown	12 (38)	13 (50)	
Target therapy in the present study, n (%)			
TACE	9 (28)	12 (46)	n.s.
TAI[a]	17 (53)	9 (35)	
RFA	1 (3)	3 (12)	
TACE+PEIT	0 (0)	1 (4)	
Systemic chemotherapy	5 (16)	1 (4)	
Clinical stage at pre-treatment, n (%)			
UICC, 6th edition			
Stage II–III	19 (59)	23 (88)	0.01[c]
Stage IV	13 (41)	3 (12)	
Milan criteria at pre-treatment, n (%)			
Fulfilled	10 (31)	10 (38)	n.s.
Beyond	22 (69)	16 (62)	
Clinical stage at post-PET evaluation, n (%)			
UICC, 6th edition			
Stage II–III	13 (41)	23 (88)	0.0001[c]
Stage IV	19 (59)	3 (12)	
Milan criteria at post-PET evaluation, n (%)			
Fulfilled	4 (13)	13 (50)	0.002[c]
Beyond	28 (88)	13 (50)	

	High FDG group (n=32)	Low FDG group (n=26)	p
Past history of therapy[a], n (%)			
Partial resection	17 (53)	12 (46)	n.s.
LDLT	1 (3)	0 (0)	
TACE	24 (75)	19 (73)	
TAI	17 (53)	14 (54)	
RFA	16 (50)	12 (46)	
PEIT	5 (16)	7 (27)	
Child-Pugh classification at PET study, n (%)			
A	21 (66)	12 (46)	0.02[c]
B	8 (25)	14 (54)	
C	3 (9)	0 (0)	
Child-Pugh score at PET study			
Mean±SD	6.3±1.6	6.6±1.1	n.s.
Pathological grade of hepatitis			
None or low	14 (44)	10 (38)	n.s.
Moderate or high	8 (25)	5 (19)	
	(n=22)	(n=15)	
Pre-therapeutic tumour markers			
αFP (ng/ml)	12,926±37,934	6,734±30,440	n.s.
αFP-L3 fraction (%)	37.2±29.9	42.6±33.8	n.s.
PIVKA-II (AU/ml)	8,666±25,900	10,093±43,296	n.s.
	(n=32)	(n=23)	
Post-therapeutic tumour markers			
αFP (ng/ml)	14,532±35,462	306±796	0.001[b]
αFP-L3 fraction (%)	38.5±28.6	35.1±31.9	n.s.
PIVKA-II (AU/ml)	9,206±34,433	531±1,938	0.005[b]
Pre-therapeutic FDG PET			
SUV	4.9±2.5	5.8±3.6	n.s.
Diagnosis: positive vs negative	10 vs 8	8 vs 3	n.s.
	(n=18)	(n=11)	
Post-therapeutic FDG PET			
SUV	7.0±4.6	2.6±0.9	0.0001[b]

[a] Including overlapping therapy

[b] Significant by Wilcoxon score

[c] Significant by chi-square

in TACE patients, in which αFP level, unilobar tumours and/or Child-Pugh score are the prognostic factors in HCC patients treated with TACE [41, 42]. Based on the evidence reported, it seems reasonable to suppose that our results in prognostic factor analysis have considerable validity. Although αFP level was the strongest, the most convenient and the less expensive prognostic factor in the present study, FDG PET has an advantage in the detection of active lesions. In addition, PET results would be helpful when the post-therapeutic αFP response was controversial. For example, in Fig. 3 post-therapeutic αFP showed a rise while PET diagnosis showed negative result. Thus, we believe that FDG PET has important clinical value in the prognostic prediction and in the decision-making process of patient management. It is to be noted that clinical staging and Milan criteria at post-PET were significant prognostic factors, while those at pre-treatment were not. It again emphasizes the importance of FDG PET diagnosis, not only for the prognostic value of its own, but also in the sense of detection of unknown metastases and the resultant renewed clinical

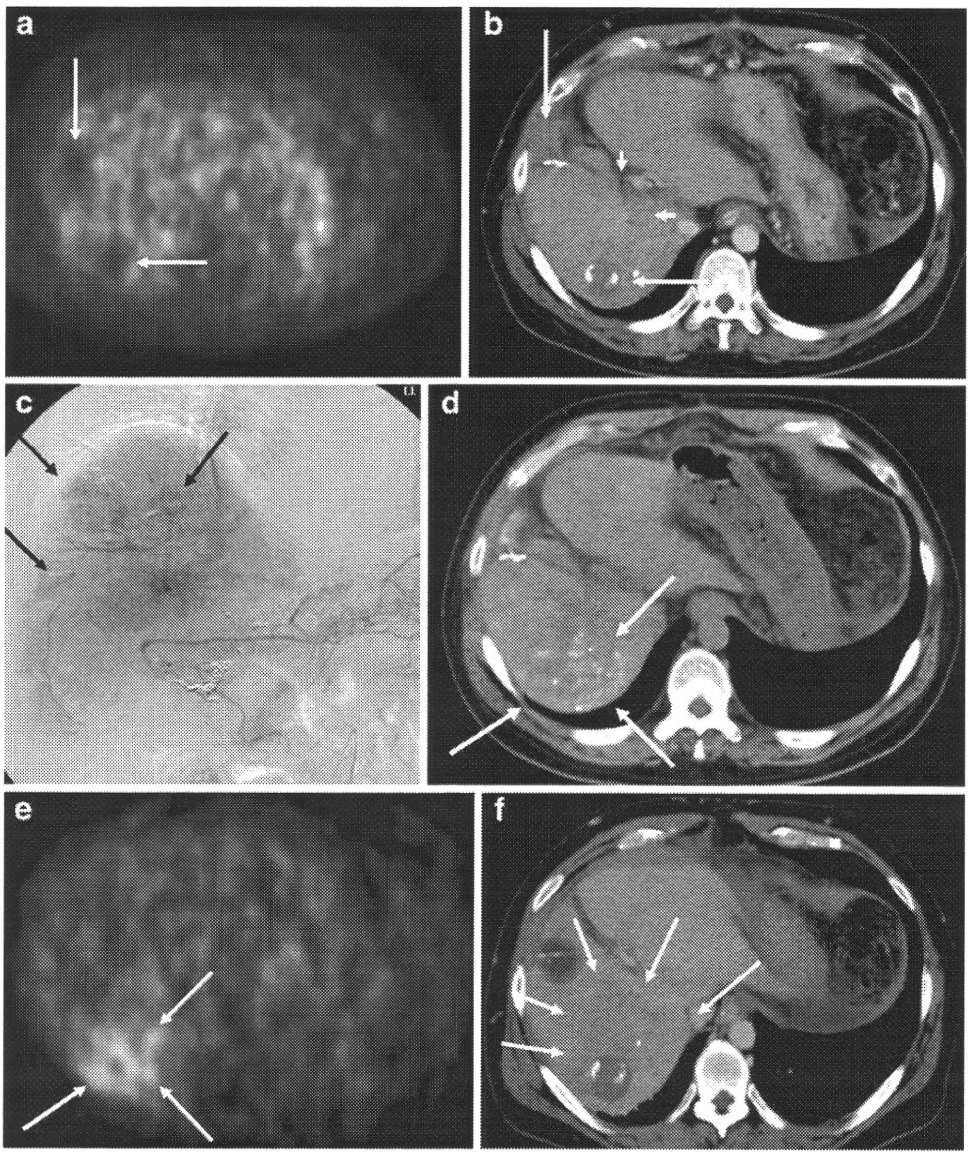

Fig. 2 A case of the L-H group: a 50-year-old man with unresectable moderately differentiated HCC, based on hepatitis type C. Past history: HCC was detected 2 years ago, and partial hepatectomy (S5) with splenectomy, TACE and RFA had been already performed. Present history: multiple recurrent nodules in bilateral lobes were detected with increased tumour markers. Then, an arterial catheter was inserted in the proper hepatic artery and TAI using biweekly infusion of CDDP and 5-FU had been performed via an indwelling arterial port. However, the arterial port was decannulated 80 days before the target TAI therapy because of the complication in the local subcutaneous tissue. **a** FDG PET was performed at 73 days before the TAI therapy. Defects of FDG uptake (*arrows*) were observed in the right lobe of the liver; therefore, visual PET diagnosis was negative at this time (SUV: 3.76 in the right posterior section). Tumour markers at this time were as follows: αFP: 632 ng/ml, αFP-L3: 53.4%, PIVKA-II: 193. **b** Follow-up contrast-enhanced CT scan was performed at 23 days before the TAI therapy. Faint enhancement at arterial phase was observed in the right posterior section (*arrowheads*) and lateral lobe (not shown). Therefore, the TAI therapy was scheduled because of these multiple nodules. Low-density areas corresponding to the defects in PET are also shown (*arrows*). **c** Angiography at the time of the non-operative therapy. Vague and faint multiple tumour stains were observed in the whole liver (*arrows*). Arterial infusion chemotherapy using one shot of water-soluble CDDP (50 mg) and lipiodol (5CC) was performed via the proper hepatic artery. **d** Follow-up plain CT scan was performed at 7 days after the TAI therapy. Scattered lipiodol deposition was observed in the right posterior section (*arrows*), which corresponded to the tumour stain at angiography. **e** FDG PET was performed at 14 days after the TAI therapy. Increased FDG uptake was observed in the right posterior section corresponding to the lipiodol deposition (SUV: 5.99) (*arrows*). Tumour markers showed a rise despite the therapy: αFP: 1860 ng/ml; αFP-L3: 46.4%; PIVKA-II: 1670. **f** Follow-up contrast-enhanced CT scan was performed at 35 days after the TAI therapy. Widespread low enhancement in the right posterior section at portal phase was clearly revealed at this CT scan (*arrows*). Since then, the recurrent HCC showed a rapid increase with portal vein tumor thrombus, and this patient died 187 days after the TAI therapy because of liver failure

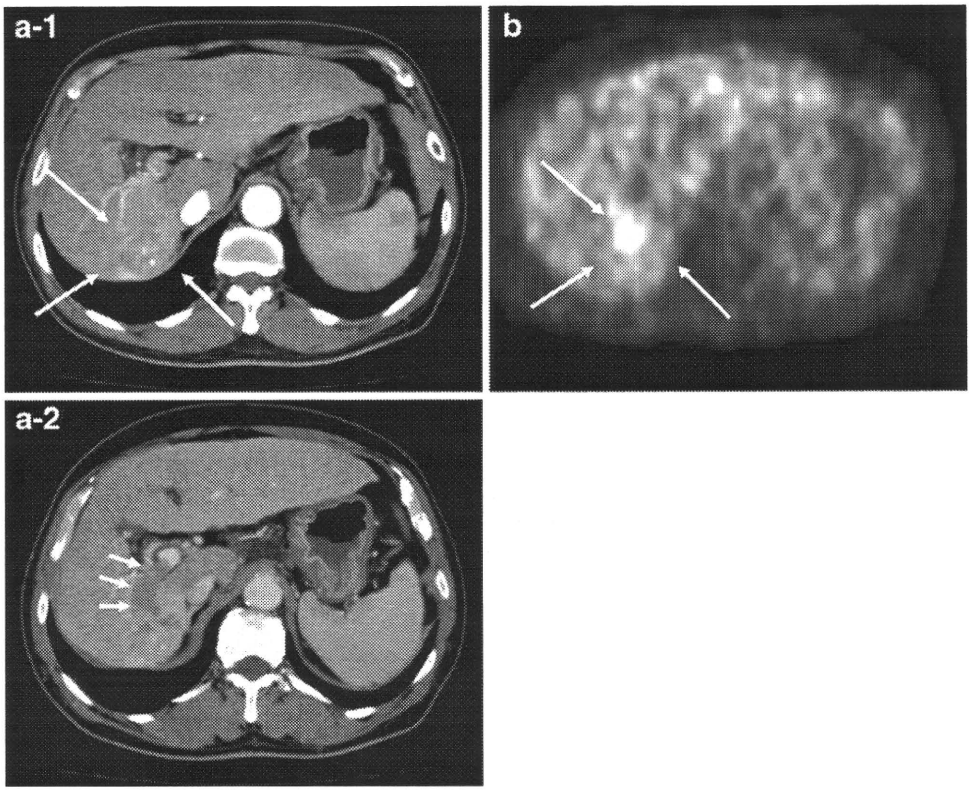

Fig. 3 A case of the H-L group: a 73-year-old man with unresectable poorly differentiated HCC, based on hepatitis type C. Past history: solitary HCC was detected 4 years ago, and RFA and TACE (twice) had been performed. Present history: post-operative HCC in the right posterior section showed local re-growth with portal vein tumour thrombus. **a** Contrast-enhanced CT scan was performed at 90 days before the start of the target TAI therapy. Solitary nodule in the right posterior section was observed with irregular hypervascularity at arterial phase (A-1) (*arrows*). CT scan at portal phase revealed that tumour thrombus reached the right main branch of the portal vein (A-2) (*arrowhead*). **b** FDG PET was performed at 88 days before the start of TAI therapy. Increased FDG uptake (*arrows*) were observed in the right posterior section of the liver; therefore, visual PET diagnosis was positive at this time (SUV: 4.89). Then, right lobectomy with resection of the portal vein tumour thrombus was performed 85 days before the TAI therapy. **c** Follow-up contrast-enhanced CT scan was performed at 40 days before the start of TAI therapy. Irregular hypervascular lesions were observed in the middle lobe and in the lateral lobe at arterial phase (C-1) (*arrows*). These lesions also showed low enhancement in the portal phase (C-2) (*arrows*). Coronal image of CT scan at portal phase revealed tumour thrombus in the left main branch of the portal vein (C-3) (*arrowhead*). Tumour markers were not so high at this time: αFP: 17 ng/ml; αFP-L3: 80.6%; PIVKA-II: 20. **d** Angiography at the time of the non-operative therapy. Multiple tumour stains were observed in the whole liver (*arrows*). An arterial catheter was inserted in the left hepatic artery and then transarterial infusion chemotherapy (TAI) was started via an indwelling arterial port using continuous infusion of low-dose CDDP and 5-FU for 3 weeks (5 days infusion with 2 days rest). **e** Contrast-enhanced CT scan was performed at 1 day after the end of the TAI therapy. An irregular hypervascular lesion in arterial phase with low enhancement in portal phase was observed almost the same area in the middle lobe (E-1, E-2) (*arrows*). Coronal image of CT scan at portal phase showed enlarged tumour thrombus in the left main branch of the portal vein (E-3) (*arrowhead*). CT diagnosis implied that TAI therapy was not effective. Tumour markers at this time also showed a rise despite the therapy: αFP: 50.9 ng/ml, αFP-L3: 78.6%, PIVKA-II: 399. **f** FDG PET was performed at 2 days after the end of the TAI therapy. No increased FDG uptake was observed in the corresponding area (SUV: 3.84 in the middle lobe), which suggested positive therapeutic effect despite the results of CT scan and tumour markers. **g** Contrast-enhanced CT scan was performed at 309 days after the end of the TAI therapy. There was no hypervascular lesion in the liver. After the TAI therapy, several TAI therapies had been continued intermittently and the multiple hepatic lesions disappeared as shown in this CT image. This patient was disease-free for 420 days after the TAI therapy, and then local recurrence was detected. He was still alive at 519 days after the TAI therapy

staging. In the present study, PET showed positive results and upgraded clinical stages in around 10% of patients.

Quantitative analysis of FDG PET using SUV was not significantly useful for the prognostic prediction in multivariate analysis. This is not compatible with the previous reports from our group [20, 21]. The reason is probably because of the difference in patient population, resectable HCC vs unresectable HCC. In the present study, not only the cases with hepatic lesions, but also the cases with distant metastasis were included for the analysis. For example, metastatic lung nodules with SUV=3.5 can be detected easily by FDG PET, while intrahepatic nodules with SUV=3.5 cannot be detected easily because of relatively higher background uptake of liver parenchyma.

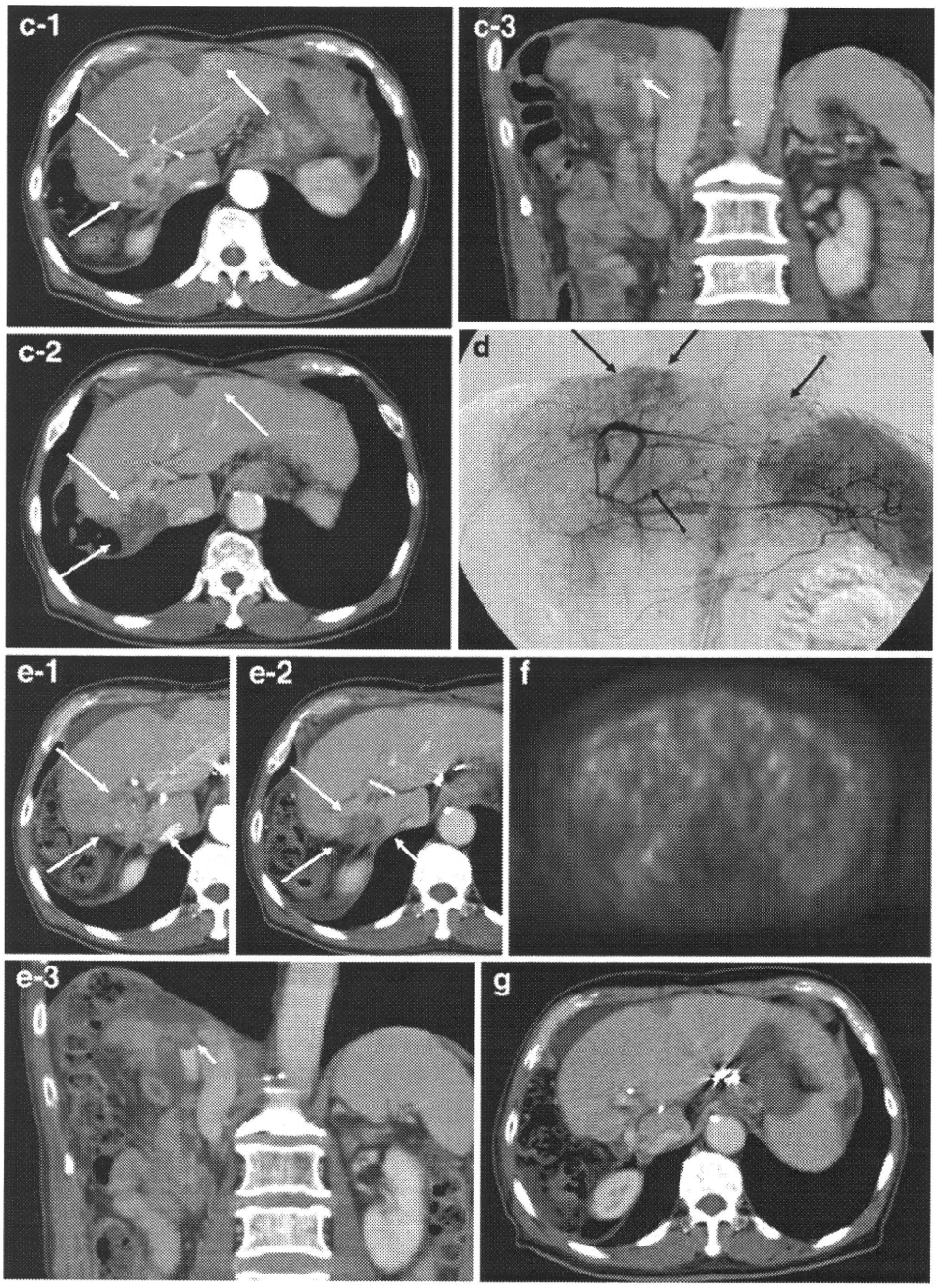

Fig. 3 (continued)

Therefore, only the factor "post-therapeutic visual PET diagnosis (positive or negative)" was statistically significant in the present study.

Limitations of the study should be discussed. First of all, there was a potential bias in the study population. Of 122 cases with unresectable HCC, only 67 cases were included in the present study. Some of the excluded cases received FDG PET 1 month after the end of non-operative therapy, while others did not receive post-therapeutic PET at all. In most cases, however, the reason why these patients did not receive PET within 1 month after the therapy was unknown. This is a limitation in a retrospective study. Secondly, the timing of post-therapeutic FDG PET might have been too early after the non-operative therapy. This was the reason why the diagnosis of lesion viability showed relatively poor results. Typically, post-therapeutic FDG PET study is supposed to be performed more than 2 weeks after the end of the chemotherapy cycle and 6–8 weeks after radiotherapy [43, 44]. Post-therapeutic PET performed more than 4 weeks after the end of non-operative therapy might be better for the diagnostic value in

the diagnosis of lesion viability. However, it can be said from our data that early performance of PET is more useful from a prognostic point of view. Post-therapeutic PET within 1 month after the end of therapy may help in making a prompt decision in patient management. Thirdly, pre-treatment FDG PET was performed in only 29 cases (50%). It means that post-therapeutic PET did not always reflect the therapeutic effect of non-operative therapy. Negative results of post-therapeutic PET can be explained not only by therapeutic effect, but also by lack of the FDG-avid character of HCC itself. This is partly the reason why diagnosis of lesion viability showed relatively poor results. However, the statistical analysis suggested that one of the most important factors for the prognosis of unresectable HCC patients treated by non-operative therapy was the result of post-therapeutic FDG uptake, not that of the pre-treatment one. From a clinical viewpoint, pre-treatment FDG PET may be omitted.

In conclusion, the present study suggests the following: (1) post-therapeutic PET performed within 1 month after non-operative therapy can be a good predictor of survival in unresectable HCC patients, (2) patients with unresectable HCC diagnosed as positive by post-therapeutic FDG PET study are highly supposed to die within 24 months, while patients diagnosed as negative are highly supposed to survive more than 12 months and (3) a negative result of post-therapeutic FDG PET study may not always mean tumour cell death, and further treatment or further clinical follow-up would be needed.

References

1. Pisani P, Parkin DM, Bray F, Ferlay J. Estimates of the worldwide mortality from 25 cancers in 1990. Int J Cancer 1999;83:18–29.
2. Röcken C, Carl-McGrath S. Pathology and pathogenesis of hepatocellular carcinoma. Dig Dis 2001;19:269–78.
3. Llovet JM, Fuster J, Bruix J. Intention-to-treat analysis of surgical treatment for early hepatocellular carcinoma: resection versus transplantation. Hepatology 1999;30:1434–40.
4. Jonas S, Bechstein WO, Steinmüller T, Herrmann M, Radke C, Berg T, et al. Vascular invasion and histopathologic grading determine outcome after liver transplantation for hepatocellular carcinoma in cirrhosis. Hepatology 2001;33:1080–6.
5. Cormier JN, Thomas KT, Chari RS, Pinson CW. Management of hepatocellular carcinoma. J Gastrointest Surg 2006;10:761–80.
6. Llovet JM, Ricci S, Mazzaferro V, Hilgard P, Gane E, Blanc JF, et al. Sorafenib in advanced hepatocellular carcinoma. N Engl J Med 2008;359:378–90.
7. Therasse P, Arbuck SG, Eisenhauer EA, Wanders J, Kaplan RS, Rubinstein L, et al. New guidelines to evaluate the response to treatment in solid tumors. European Organization for Research and Treatment of Cancer, National Cancer Institute of the United States, National Cancer Institute of Canada. J Natl Cancer Inst 2000;92:205–16.
8. Johnson PJ. Hepatocellular carcinoma: is current therapy really altering outcome? Gut 2002;51:459–62.
9. Llovet JM, Brú C, Bruix J. Prognosis of hepatocellular carcinoma: the BCLC staging classification. Semin Liver Dis 1999;19:329–38.
10. Imamura H, Matsuyama Y, Tanaka E, Ohkubo T, Hasegawa K, Miyagawa S, et al. Risk factors contributing to early and late phase intrahepatic recurrence of hepatocellular carcinoma after hepatectomy. J Hepatol 2003;38:200–7.
11. Okazumi S, Isono K, Enomoto K, Kikuchi T, Ozaki M, Yamamoto H, et al. Evaluation of liver tumors using fluorine-18-fluorodeoxyglucose PET: characterization of tumor and assessment of effect of treatment. J Nucl Med 1992;33:333–9.
12. Schröder O, Trojan J, Zeuzem S, Baum RP. Limited value of fluorine-18-fluorodeoxyglucose PET for the differential diagnosis of focal liver lesions in patients with chronic hepatitis C virus infection. Nuklearmedizin 1998;37:279–85.
13. Torizuka T, Tamaki N, Inokuma T, Magata Y, Yonekura Y, Tanaka A, et al. Value of fluorine-18-FDG-PET to monitor hepatocellular carcinoma after interventional therapy. J Nucl Med 1994;35:1965–9.
14. Torizuka T, Tamaki N, Inokuma T, Magata Y, Sasayama S, Yonekura Y, et al. In vivo assessment of glucose metabolism in hepatocellular carcinoma with FDG-PET. J Nucl Med 1995;36:1811–7.
15. Shiomi S, Nishiguchi S, Ishizu H, Iwata Y, Sasaki N, Tamori A, et al. Usefulness of positron emission tomography with fluorine-18-fluorodeoxyglucose for predicting outcome in patients with hepatocellular carcinoma. Am J Gastroenterol 2001;96:1877–80.
16. Delbeke D, Martin WH, Sandler MP, Chapman WC, Wright JK Jr, Pinson CW. Evaluation of benign vs malignant hepatic lesions with positron emission tomography. Arch Surg 1998;133:510–5.
17. Trojan J, Schroeder O, Raedle J, Baum RP, Herrmann G, Jacobi V, et al. Fluorine-18 FDG positron emission tomography for imaging of hepatocellular carcinoma. Am J Gastroenterol 1999;94:3314–9.
18. Khan MA, Combs CS, Brunt EM, Lowe VJ, Wolverson MK, Solomon H, et al. Positron emission tomography scanning in the evaluation of hepatocellular carcinoma. J Hepatol 2000;32:792–7.
19. Jeng LB, Changlai SP, Shen YY, Lin CC, Tsai CH, Kao CH. Limited value of 18F-2-deoxyglucose positron emission tomography to detect hepatocellular carcinoma in hepatitis B virus carriers. Hepatogastroenterology 2003;50:2154–6.
20. Hatano E, Ikai I, Higashi T, Teramukai S, Torizuka T, Saga T, et al. Preoperative positron emission tomography with fluorine-18-fluorodeoxyglucose is predictive of prognosis in patients with hepatocellular carcinoma after resection. World J Surg 2006;30:1736–41.
21. Seo S, Hatano E, Higashi T, Hara T, Tada M, Tamaki N, et al. Fluorine-18 fluorodeoxyglucose positron emission tomography predicts tumor differentiation, P-glycoprotein expression, and outcome after resection in hepatocellular carcinoma. Clin Cancer Res 2007;13:427–33.
22. International Union Against Cancer (UICC). TNM classification of malignant tumours. 6th ed. New York: Wiley-Liss; 2002.
23. Mazzaferro V, Rondinara GF, Rossi G, Regalia E, De Carlis L, Caccamo L, et al. Milan multicenter experience in liver transplantation for hepatocellular carcinoma. Transplant Proc 1994;26:3557–60.
24. Ito T, Takada Y, Ueda M, Haga H, Maetani Y, Oike F, et al. Expansion of selection criteria for patients with hepatocellular carcinoma in living donor liver transplantation. Liver Transpl 2007;13:1637–44.
25. Toyoda H, Kumada T, Osaki Y, Oka H, Urano F, Kudo M, et al. Staging hepatocellular carcinoma by a novel scoring system (BALAD score) based on serum markers. Clin Gastroenterol Hepatol 2006;4:1528–36.
26. Higashi T, Saga T, Nakamoto Y, Ishimori T, Fujimoto K, Doi R, et al. Diagnosis of pancreatic cancer using fluorine-18 fluorodeoxyglucose positron emission tomography (FDG PET)—usefulness and limitations in "clinical reality". Ann Nucl Med 2003;17:261–79.
27. Delbeke D, Martin WH. PET and PET-CT for evaluation of colorectal carcinoma. Semin Nucl Med 2004;34:209–23.

28. Weber WA. Use of PET for monitoring cancer therapy and for predicting outcome. J Nucl Med 2005;46:983–95.
29. Specht L. 2-[18F]fluoro-2-deoxyglucose positron-emission tomography in staging, response evaluation, and treatment planning of lymphomas. Semin Radiat Oncol 2007;17:190–7.
30. Caracó C, Aloj L, Chen LY, Chou JY, Eckelman WC. Cellular release of [18F]2-fluoro-2-deoxyglucose as a function of the glucose-6-phosphatase enzyme system. J Biol Chem 2000;275: 18489–94.
31. Jinno K, Moriwaki S, Tanada M, Wada T, Mandai K, Okada Y. Clinicopathological study on combination therapy consisting of arterial infusion of lipiodol-dissolved SMANCS and transcatheter arterial embolization for hepatocellular carcinoma. Cancer Chemother Pharmacol 1992;31(Suppl):S7–12.
32. Livraghi T. Radiofrequency ablation, PEIT, and TACE for hepatocellular carcinoma. J Hepatobiliary Pancreat Surg 2003; 10:67–76.
33. Geschwind JF, Ramsey DE, Choti MA, Thuluvath PJ, Huncharek MS. Chemoembolization of hepatocellular carcinoma: results of a meta-analysis. Am J Clin Oncol 2003;26:344–9.
34. Kong G, Jackson C, Koh DM, Lewington V, Sharma B, Brown G, et al. The use of 18F-FDG PET/CT in colorectal liver metastases—comparison with CT and liver MRI. Eur J Nucl Med Mol Imaging 2008;35:1323–9.
35. Cascini GL, Avallone A, Delrio P, Guida C, Tatangelo F, Marone P, et al. 18F-FDG PET is an early predictor of pathologic tumor response to preoperative radiochemotherapy in locally advanced rectal cancer. J Nucl Med 2006;47:1241–8.
36. Naumann R, Vaic A, Beuthien-Baumann B, Bredow J, Kropp J, Kittner T, et al. Prognostic value of positron emission tomography in the evaluation of post-treatment residual mass in patients with Hodgkin's disease and non-Hodgkin's lymphoma. Br J Haematol 2001;115:793–800.
37. Prior JO, Montemurro M, Orcurto MV, Michielin O, Luthi F, Benhattar J, et al. Early prediction of response to sunitinib after imatinib failure by 18F-fluorodeoxyglucose positron emission tomography in patients with gastrointestinal stromal tumor. J Clin Oncol 2009;27:439–45.
38. Rousseau C, Devillers A, Sagan C, Ferrer L, Bridji B, Campion L, et al. Monitoring of early response to neoadjuvant chemotherapy in stage II and III breast cancer by [18F]fluorodeoxyglucose positron emission tomography. J Clin Oncol 2006;24:5366–72.
39. Miyaaki H, Nakashima O, Kurogi M, Eguchi K, Kojiro M. Lens culinaris agglutinin-reactive alpha-fetoprotein and protein induced by vitamin K absence II are potential indicators of a poor prognosis: a histopathological study of surgically resected hepatocellular carcinoma. J Gastroenterol 2007;42:962–8.
40. De Carlis L, Giacomoni A, Lauterio A, Slim A, Sammartino C, Pirotta V, et al. Liver transplantation for hepatocellular cancer: should the current indication criteria be changed? Transpl Int 2003;16:115–22.
41. O'Suilleabhain CB, Poon RT, Yong JL, Ooi GC, Tso WK, Fan ST. Factors predictive of 5-year survival after transarterial chemoembolization for inoperable hepatocellular carcinoma. Br J Surg 2003;90:325–31.
42. Doffoël M, Bonnetain F, Bouché O, Vetter D, Abergel A, Fratté S, et al. Multicentre randomised phase III trial comparing Tamoxifen alone or with Transarterial Lipiodol Chemoembolisation for unresectable hepatocellular carcinoma in cirrhotic patients (Fédération Francophone de Cancérologie Digestive 9402). Eur J Cancer 2008;44:528–38.
43. Young H, Baum R, Cremerius U, Herholz K, Hoekstra O, Lammertsma AA, et al. Measurement of clinical and subclinical tumour response using [18F]-fluorodeoxyglucose and positron emission tomography: review and 1999 EORTC recommendations. European Organization for Research and Treatment of Cancer (EORTC) PET Study Group. Eur J Cancer 1999;35:1773–82.
44. Shankar LK, Hoffman JM, Bacharach S, Graham MM, Karp J, Lammertsma AA, et al. Consensus recommendations for the use of 18F-FDG PET as an indicator of therapeutic response in patients in National Cancer Institute Trials. J Nucl Med 2006; 47:1059–66.

Technical Note

Visualization of External Carotid Artery and Its Branches: Non–contrast-Enhanced MR Angiography Using Balanced Steady-State Free-Precession Sequence and a Time-Spatial Labeling Inversion Pulse

Naoe Satogami, MD, Tomohisa Okada, MD, PhD,* Takashi Koyama, MD, PhD, Kimio Gotoh, MD, Toshikazu Kamae, MS, RT, and Kaori Togashi, MD, PhD

Purpose: To evaluate visibility of the external carotid artery (ECA) and its branches using three-dimensional (3D) balanced steady-state free-precession (SSFP) MR angiography with a time-spatial labeling inversion pulse (Time-SLIP), and to provide an optimal value of the inversion time (TI).

Materials and Methods: Peripheral-pulse-wave-gated 3D balanced SSFP images were obtained in 20 healthy volunteers. Images with a Time-SLIP using four different TIs (600, 900, 1200, and 1500 ms) and without a Time-SLIP, referred to as sequence A to E, were acquired for each subject and compared for visibility scores of ECA system and relative signal intensity (SI) of ECA.

Results: Average Friedman rank for overall visibility was 1.63, 3.01, 3.59, 3.58, and 3.20 for sequence A to E, respectively. Sequence C and D yielded significantly higher visibility than sequence A, B, and E. The mean relative SI value was 0.97, 0.87, 0.81, 0.76, and 0.67 for sequence A to E, respectively.

Conclusion: Balanced SSFP MR angiography with a Time-SLIP is superior to that without a Time-SLIP, showing excellent visualization of ECA system in approximately 3 min in average with sufficient background suppression including veins and salivary ducts. A TI of 1200 ms was considered to be optimal for this purpose.

Key Words: MR angiography; non–contrast-enhanced; external carotid artery; time-spatial labeling inversion pulse; balanced steady-state free-precession
J. Magn. Reson. Imaging 2009;30:678–683.

ANATOMICAL INFORMATION OF the external carotid artery (ECA) system has become more important for less-invasive treatment approaches to head and neck disorders (1–4), and time-of-flight (TOF) and phase-contrast (PC) imaging have been used for non–contrast-enhanced head and neck MR angiography (MRA) (5). However, saturation effects often lead to signal reduction of the ECA branches in TOF. In PC, motion artifacts caused by a long acquisition time can produce poor visualization of peripheral or movable branches, although the combined use of the parallel imaging and PC has shown good depiction of the ECA system (6).

Recently balanced steady-state free-precession (SSFP) sequence (also referred to as true fast imaging with steady-state precession [true FISP], fast imaging employing steady-state acquisition [FIESTA], balanced turbo field echo [bTFE], or true SSFP) has been applied to non–contrast-enhanced MRA of various regions including the coronary artery and hepatic vessels (7–9). Relatively good visualization of the ECA branches with balanced SSFP has been reported in face and neck region (6,10). However, veins and salivary gland ducts also show high signal intensity in this sequence, which becomes problematic for vessel identification, especially in maximum intensity projection (MIP) images.

To overcome this problem, the time-spatial labeling inversion pulse (Time-SLIP) method can be adopted, although there have been no reports in the literature regarding visibility of the ECA branches with use of Time-SLIP, to the best of our knowledge. It applies a selective inversion pulse before data acquisition and suppresses the background signal, thus provides selective blood inflow information (7). The alteration of the inversion time (TI) in Time-SLIP can control the extent of inflowing arterial signal and background signal suppression. The purpose of this study was to evaluate visibility of the ECA and its branches using balanced SSFP imaging with a Time-SLIP, and provide an optimal TI value for this protocol.

MATERIALS AND METHODS

Subjects

Twenty healthy volunteers (14 men and 6 women; mean age, 24 years; age range, 18–31 years) were included in this study, which was approved by the local ethics com-

Department of Diagnostic Imaging and Nuclear Medicine, Kyoto University Graduate School of Medicine, Kyoto, Japan.
Contract grant sponsor: R&D of Molecular Imaging Equipment for Malignant Tumor Therapy Support, supported by NEDO (New Energy and Industrial Technology Development Organization), Japan.
*Address reprint requests to: T.O., Department of Diagnostic Imaging and Nuclear Medicine, Kyoto University Graduate School of Medicine, 54 Kawahara-cho, Shogoin, Sakyo-ku, Kyoto 606-8507, Japan. E-mail: tomokada@kuhp.kyoto-u.ac.jp
Received March 7, 2009; Accepted June 12, 2009.
DOI 10.1002/jmri.21883
Published online in Wiley InterScience (www.interscience.wiley.com).

mittee. All subjects provided written informed consent before the examination.

MR Imaging

All MR examinations were conducted using a 1.5 Tesla (T) MR scanner (EXCELART Vantage, powered by Atlas; Toshiba Medical Systems, Tokyo, Japan) with a head and neck coil and the uppermost row of a spine coil. Before MRA acquisition, a peripheral-pulse-wave-gated preparation scan was performed to select a proper delay time from a pulse-wave trigger. Several coronal SSFP images at different times from the trigger were acquired with the following parameters: repetition time (TR), 4.2 ms; echo time (TE), 2.1 ms; flip angle, 63 degree; field of view (FOV), 225 × 300 mm; matrix, 192 × 256; slice thickness, 10 mm; slice number, 3; acquisition time, 51 s in average. An appropriate delay time was visually selected for each subject to avoid signal void by arterial flow.

For MRA, peripheral-pulse-wave-gated three-dimensional (3D) balanced SSFP images with fat saturation were obtained in coronal plane. Imaging parameters were as follows: TR, 4.3 ms; TE, 2.2 ms; flip angle, 120 degree; FOV, 180 × 320 mm; matrix, 144 × 256; slice thickness, 1.5 mm; slice number, 54; number of acquisition, 1; parallel imaging factor, 2 in the phase encoding direction. The raw data was zero-filled and final apparent resolution was 0.6 × 0.6 × 0.75 mm. The posterior border of the FOV was located approximately at the posterior edge of the vertebral body of the upper cervical spine (Fig. 1). For each subject, five balanced SSFP sequences were performed: balanced SSFP with a Time-SLIP using four different TIs (600, 900, 1200, and 1500 ms) and balanced SSFP without a Time-SLIP. The acquisition time for each sequence ranged from 1 min 50 s to 4 min 15 s (mean, 3 min 13 s) according to pulse rates of the subjects.

In balanced SSFP sequences with a Time-SLIP, a spatially selective inversion-recovery pulse with 230-mm width was placed above the inferior edge of the mandible (Fig. 1). After each TI, inflowing arterial signal was depicted as bright-blood with variable background signal suppression above the distal common carotid artery, covering the ECA system.

Image Analysis

The five MRA sequences were referred to as sequence A (TI of 600 ms), sequence B (TI of 900 ms), sequence C (TI of 1200 ms), sequence D (TI of 1500 ms), and sequence E (without a Time-SLIP). MIP images were reconstructed from the coronal source images of each sequence into 40 projections rotating around the craniocaudal axis at 9-degree increments. All qualitative and quantitative imaging evaluations were performed using OsiriX Medical Imaging Software (http://www.osirix-viewer.com/).

Qualitative Evaluation

The acquired images were assessed in two ways: "MIP" evaluation (with MIP images only) and "source" evaluation (with both MIP images and coronal source images).

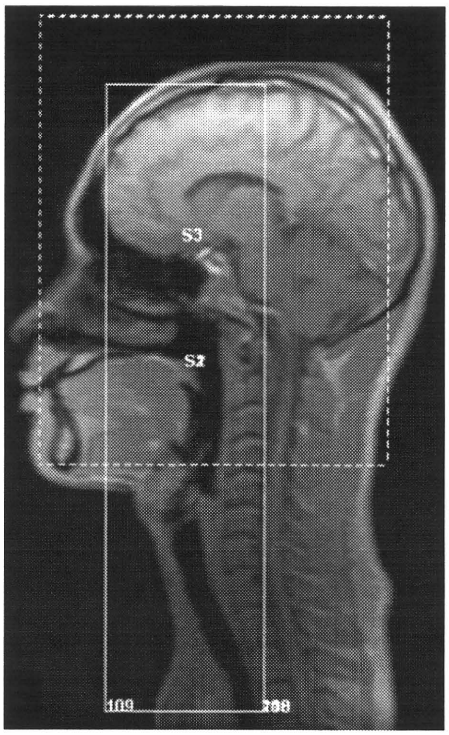

Figure 1. A representative scout image with scan planning. The posterior border of the imaged area (continuous line) is located approximately at the posterior edge of the vertebral body of the upper cervical spine. The inferior border of the inversion pulse (dotted line) is placed near the inferior edge of the mandible.

In "MIP" evaluation, a total of nine segments of the ECA system: the main ECA and eight first-order branches (the superior thyroid, lingual, facial, ascending pharyngeal, occipital, posterior auricular, maxillary, and superficial temporal artery), were evaluated for sequences A, B, C, and D. Sequence E (without a Time-SLIP) was not evaluated because separation of arteries from veins and salivary gland ducts was difficult with MIP images only. In "source" evaluation, a total of 11 segments of the ECA system: the main ECA, 8 first-order branches, and 2 second-order branches (the middle meningeal and deep lingual artery), were evaluated for sequences A, B, C, D, and E. These two second-order branches were selected for the evaluation because they showed relatively good visibility in a previous study (6), and were completely covered in the FOV in our study.

For both evaluations, two radiologists (N.S. with 7 years of experience and K.G. with 6 years of experience) independently scored visibility of each ECA segment. Visualization quality was scored on a 4-point scale: 1, not visible; 2, poor image quality, visibility of only the origin of the segment; 3, moderate image quality, visibility of the proximal portion of the segment; and 4, good image quality, visibility of the complete course of the segment. The right and left sides were separately scored. The complete course of several ECA branches, especially the occipital and posterior auricular artery, was not covered in some subjects because of FOV constraints, and these segments were scored as 4 for de-

Table 1
Mean Visibility Scores of the External Carotid Segments in "MIP" Evaluation*

	Sequence A (TI of 600 ms)	Sequence B (TI of 900 ms)	Sequence C (TI of 1200 ms)	Sequence D (TI of 1500 ms)
External carotid	3.8 ± 0.3	4.0 ± 0.0	4.0 ± 0.0	4.0 ± 0.0
Superior thyroid	2.2 ± 0.7	3.1 ± 0.6	3.4 ± 0.7	3.3 ± 0.9
Lingual	2.3 ± 0.5	3.4 ± 0.6	3.9 ± 0.3	3.9 ± 0.2
Facial	2.7 ± 0.8	3.6 ± 0.6	3.9 ± 0.4	3.9 ± 0.4
Ascending pharyngeal	1.1 ± 0.2	1.4 ± 0.7	1.7 ± 1.0	1.5 ± 0.9
Occipital	3.7 ± 0.8	3.9 ± 0.3	4.0 ± 0.1	3.9 ± 0.5
Posterior auricular	1.3 ± 0.8	2.7 ± 1.3	3.0 ± 1.2	2.6 ± 1.4
Maxillary	2.2 ± 0.6	3.3 ± 0.7	3.9 ± 0.3	3.9 ± 0.2
Superficial temporal	2.2 ± 0.7	3.5 ± 0.7	3.9 ± 0.2	4.0 ± 0.1
Average Friedman rank	1.51	2.53	3.02[a]	2.94[a]

*No significant difference is observed between sequences C and D ($P = 0.201$).
[a]$P < 0.001$ by pair-wise comparisons with sequences A and B.

scriptive purposes when they were entirely visualized in the applied FOV. "MIP" and "source" evaluations were performed separately with random orders. In "MIP" evaluation each observer scored 18 segments for each sequence in 20 subjects, constituting a total of 1440 segments. In "source" evaluation each observer scored 22 segments for each sequence in 20 subjects, constituting a total of 2200 segments.

Quantitative Evaluation

Relative signal intensity (SI) of the target organ compared with that of reference tissue was adopted for quantitative evaluation (11), because the conventionally used method to determine the signal-to-noise ratio (SNR), which is derived from two separate regions of interest (ROIs) in a single image, was difficult to apply due to the use of the parallel imaging (12). The SI of the ECA was compared with that of the muscle adjacent to it for all sequences. The average SI of the main ECA and the sternocleidomastoid muscle were measured by applying oval ROIs on the coronal source images. An ROI was manually placed at the origin of the main ECA on the right side. If the lumen of the artery showed marked heterogeneous intensity due to flow related effect, an ROI was placed at the origin of the contralateral (left) ECA. Another ROI was placed at the belly of the sternocleidomastoid muscle with homogenous signal intensity on the same side as the ROI of the artery. In each subject, ROIs of the artery were of the same shape and area for all MRA sequences and were placed on the same side and position of the main ECA; ditto with ROIs of the muscle. The range of the area of ROIs was 15–17 mm^2 for the ECA and 30–33 mm^2 for the sternocleidomastoid muscle, respectively. The relative SI, that is, the artery–muscle contrast was calculated by the following equation: relative $SI = (SI_{artery} - SI_{muscle}) / SI_{artery}$.

Statistical Analysis

All statistical analyses were conducted using SPSS software, version 12.0 (SPSS, Inc., Chicago, IL). For qualitative assessment, the degree of interobserver agreement was calculated using the Cohen's kappa test (a value of 0.21–0.40, fair agreement; 0.41–0.60, moderate agreement; 0.61–0.80, substantial agreement; 0.81–1.00, excellent agreement). Based on this result, all statistical analyses were performed using an average score of two readers for each segment. Friedman's nonparametric test was used to evaluate intersequence differences in visibility of the ECA system. A P value of less than 0.05 was considered to indicate a statistically significant difference. Wilcoxon signed-rank test with Bonferroni correction was applied for multiple pair-wise comparisons. A P value of less than 0.009 and 0.005 was considered to indicate a statistically significant difference in "MIP" evaluation and "source" evaluation, respectively.

For quantitative assessment, one-way repeated-measures analysis of variance (ANOVA) was performed for the assessment of intersequence differences in the relative SI. Scheffe's test was applied as post hoc testing for multiple comparisons. A P value of less than 0.05 was considered to indicate a statistically significant difference.

RESULTS

Qualitative Analysis

The Cohen's kappa test showed nearly almost perfect interreader agreement for "MIP" evaluation (kappa = 0.80) as well as "source" evaluation (kappa = 0.79). The scores for visibility of the ECA segments and average Friedman rank of each sequence for "MIP" and "source" evaluations were summarized in Tables 1 and 2, respectively. The Friedman's nonparametric test showed significant differences both in "MIP" and "source" evaluations ($P < 0.001$). In "MIP" evaluation, sequence A revealed the lowest values compared with the other sequences ($P < 0.001$). The scores of sequence B also showed significant deterioration in comparison with sequences C and D ($P < 0.001$). No significant difference was observed between sequence C and D ($P = 0.201$), although sequence C had slightly higher average Friedman rank (Figs. 2, 3). In "source" evaluation, visibility was significantly deteriorated in sequence A in comparison with the others ($P < 0.001$). The scores between sequence B and E revealed no significant difference ($P = 0.108$), but both sequence B and E yielded lower values compared with sequence C and D ($P < 0.001$). The scores of sequences C and D did not differ ($P = 0.961$).

Table 2
Mean Visibility Scores of the External Carotid Segments in "Source" Evaluation*

	Sequence A (TI of 600 ms)	Sequence B (TI of 900 ms)	Sequence C (TI of 1200 ms)	Sequence D (TI of 1500 ms)	Sequence E (without a Time-SLIP)
External carotid	3.9 ± 0.2	4.0 ± 0.0	4.0 ± 0.0	4.0 ± 0.0	4.0 ± 0.0
Superior thyroid	2.6 ± 0.6	3.3 ± 0.6	3.6 ± 0.6	3.7 ± 0.6	3.4 ± 0.9
Lingual	2.6 ± 0.5	3.7 ± 0.4	4.0 ± 0.2	4.0 ± 0.1	4.0 ± 0.0
Facial	3.1 ± 0.7	3.8 ± 0.5	3.9 ± 0.3	4.0 ± 0.3	3.9 ± 0.3
Ascending pharyngeal	1.6 ± 0.6	2.5 ± 0.9	2.9 ± 1.0	2.6 ± 1.1	2.0 ± 1.1
Occipital	4.0 ± 0.1	4.0 ± 0.0	4.0 ± 0.0	4.0 ± 0.0	4.0 ± 0.1
Posterior auricular	2.3 ± 1.1	3.4 ± 0.9	3.7 ± 0.7	3.6 ± 0.9	3.1 ± 1.2
Maxillary	2.6 ± 0.6	3.6 ± 0.5	3.9 ± 0.3	4.0 ± 0.1	3.8 ± 0.5
Superficial temporal	2.9 ± 0.6	3.8 ± 0.5	4.0 ± 0.0	4.0 ± 0.0	4.0 ± 0.1
Middle meningeal	1.8 ± 0.7	3.3 ± 0.8	3.8 ± 0.5	3.6 ± 0.6	2.5 ± 0.9
Deep lingual	1.1 ± 0.3	2.5 ± 1.1	3.7 ± 0.6	3.9 ± 0.3	4.0 ± 0.2
Average Friedman rank	1.63	3.01[a]	3.59[a,b]	3.58[a,b]	3.20[a]

*No significant difference is observed between sequences C and D ($P = 0.961$).
[a]$P < 0.001$ by pair-wise comparisons with sequence A.
[b]$P < 0.001$ by pair-wise comparisons with sequence B or E.

Quantitative Analysis

The relative SI values were 0.97 ± 0.02, 0.87 ± 0.02, 0.81 ± 0.02, 0.76 ± 0.02, and 0.67 ± 0.03 (mean ± standard deviation) for sequence A, B, C, D, and E, respectively. The relative SI values were largest with sequence A, second largest with sequence B, third largest with sequence C, fourth largest with sequence D, and lowest with sequence E ($P < 0.001$ for all pair-wise comparisons).

DISCUSSION

Several less-invasive treatment approaches using catheter-directed selective angiographic techniques have been more and more applied to head and neck diseases, including selective arterial embolization (1), preoperative endovascular embolization (2,3), and selective intra-arterial infusion chemotherapy (4). Detailed preoperative anatomical information of the ECA system is especially important for these treatment approaches.

Contrast-enhanced MRA has been applied to the ECA system and high-resolution images can be obtained especially on 3T MRI units (13), although it has some disadvantages such as potential nephrotoxicity and association with nephrogenic systemic fibrosis (14). Computed tomography angiography can also be used for the external carotid evaluation (15), but radiation exposure is inevitable and iodine-based contrast materials are potentially nephrotoxic (16) and have a relatively high risk of allergic adverse reactions (17).

Recently Sumi et al (6) applied balanced SSFP sequence to MRA of the ECA system. Balanced SSFP is a special type of rapid gradient-echo sequence in which the imaging gradients are fully balanced without an influence on the transverse magnetization (18). This sequence provides a rapid imaging with a very high SNR, and the intrinsic image contrast is determined by T2/T1 ratio of the tissue. A strong contrast between the blood vessels and muscle can be obtained, but veins and salivary gland ducts as well as arteries show high signal intensity. Sumi et al (6) stated that an effective method of separating arteries from veins and salivary gland ducts was needed for balanced SSFP MRA.

The time-SLIP technique is a useful method to depict arteries selectively with good background signal suppression without use of contrast materials (19), and it can be applied to balanced SSFP. A spatially selective inversion-recovery pulse is placed before data acquisition, and blood inflowing into the desired imaging area during an inversion time is depicted as bright while suppressed background signal is gradually recovering. Better background suppression and less peripheral branch depiction are observed with a shorter TI, while a longer TI enables better visualization of peripheral branches although background signal recovery may mask inflowing blood signal. Concerning an optimal TI value of the current study, sequence C (TI of 1200 ms) and D (TI of 1500 ms) showed higher visibility compared with sequence A and B in both "MIP" and "source" evaluations. Better background suppression, that is, a higher relative SI value was observed in sequence C compared with sequence D, and a TI of 1200 ms was suggested to be an optimal value in our protocol.

Theoretically, balanced SSFP with a Time-SLIP cannot visualize the entire ECA system to the same level as that without a Time-SLIP on the source images, because a spatially selective inversion-recovery pulse suppresses arterial signal in the imaged area to some extent. However, our results showed that balanced SSFP with a time-SLIP with a relatively long TI (sequence C and D) showed higher visibility than sequence E even in "source" evaluation. Better background suppression including veins and salivary gland ducts may help more confident identification and tracking of the ECA segments.

There are several limitations in our study. First, conventional angiography was not performed in any subjects, which would have been a reference standard for the anatomical evaluation. However, most ECA branches could be identified with confidence in our study, and our main purpose was the optimization of the imaging protocols. Second, balanced SSFP MRA with a Time-SLIP was not compared with PC MRA. Sumi

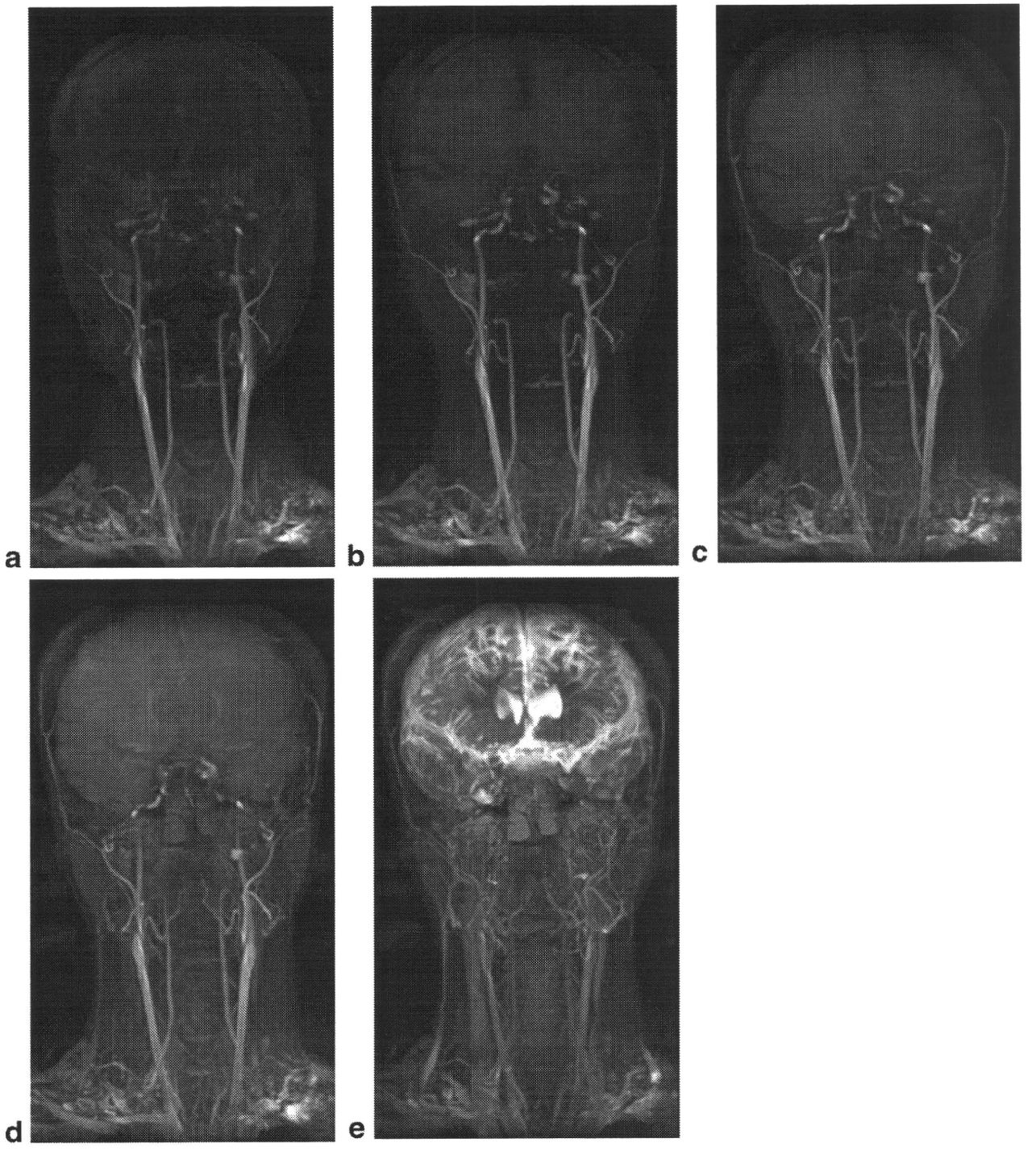

Figure 2. Visualization of the external carotid artery system with different TIs (coronal MIP images of a 25-year-old man). **a–e:** Sequences A–D with a Time-SLIP using a TI of 600 (a), 900 (b), 1200 (c), and 1500 (d) ms, and sequence E (e, without a Time-SLIP). Background signal was better suppressed for shorter TIs (see a,b), but more peripheral branches were visualized with the increase of TI (see c,d). Note complicated signals without a Time-SLIP (e).

et al (6) reported that PC with the parallel imaging performed the best for overall visibility of the ECA system among TOF, PC, and balanced SSFP, although arterial spin-labeling method was not used in their study. We did not assess PC MRA because the parallel imaging was not available for PC sequence in the MR scanner used in this study. Another limitation is that a time-resolved display of the neovascularization of tumors that is enabled by using contrast-enhancement (20) is not capable in the current method.

In conclusion, this is the first report evaluating visibility of the external carotid artery and its branches in balanced SSFP sequence with the Time-SLIP method, to the best of our knowledge. Balanced SSFP MRA with a Time-SLIP allows excellent visualization of the external carotid artery system in around 3 min with sufficient

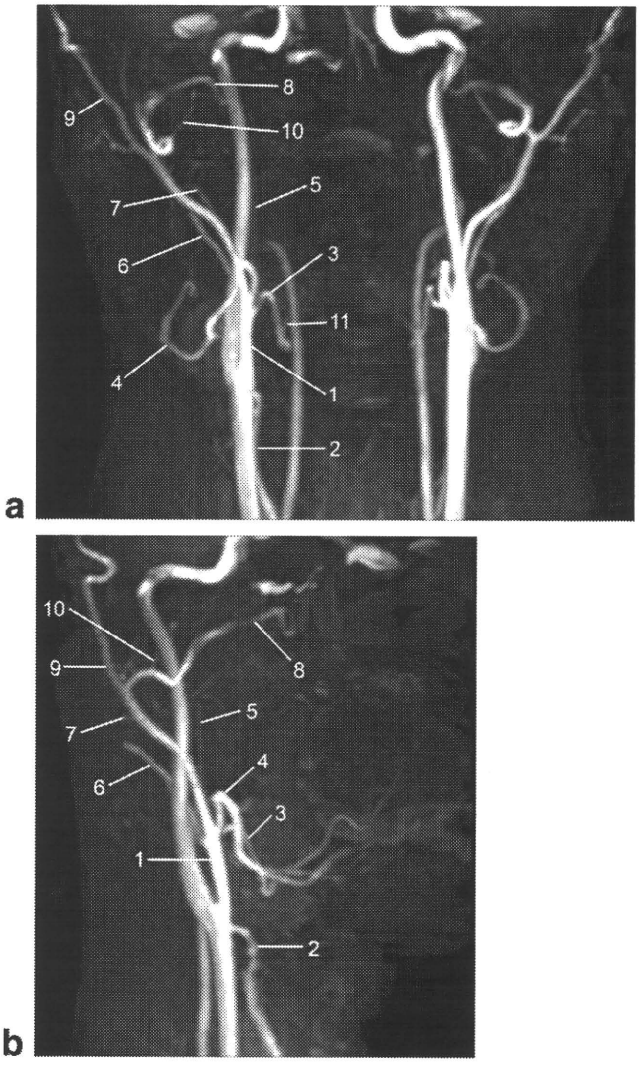

Figure 3. Balanced SSFP MR angiography of the external carotid artery system with a Time-SLIP using the optimal TI of 1200 ms in a 23-year-old man. **a,b:** Coronal (a) and oblique-lateral (b) MIP images. Good visualization was obtained for the external carotid artery and its branches: (1) the main external carotid artery, (2) superior thyroid artery, (3) lingual artery, (4) facial artery, (5) ascending pharyngeal artery, (6) occipital artery, (7) posterior auricular artery, (8) maxillary artery, (9) superficial temporal artery, (10) middle meningeal artery, and (11) deep lingual artery.

background signal suppression inclusive of veins and salivary gland ducts. A TI of 1200 ms was considered to be optimal for this purpose.

REFERENCES

1. Elden L, Montanera W, Terbrugge K, Willinsky R, Lasjaunias P, Charles D. Angiographic embolization for the treatment of epistaxis: a review of 108 cases. Otolaryngol Head Neck Surg 1994; 111:44–50.
2. Marshall AH, Bradley PJ. Management dilemmas in the treatment and follow-up of advanced juvenile nasopharyngeal angiofibroma. ORL J Otorhinolaryngol Relat Spec 2006;68:273–278.
3. Kasper GC, Welling RE, Wladis AR, et al. A multidisciplinary approach to carotid paragangliomas. Vasc Endovascular Surg 2006; 40:467–474.
4. Tsurumaru D, Kuroiwa T, Yabuuchi H, Hirata H, Higaki Y, Tomita K. Efficacy of intra-arterial infusion chemotherapy for head and neck cancers using coaxial catheter technique: initial experience. Cardiovasc Intervent Radiol 2007;30:207–211.
5. van den Berg R, Wasser MN, van Gils AP, van der Mey AG, Hermans J, van Buchem MA. Vascularization of head and neck paragangliomas: comparison of three MR angiographic techniques with digital subtraction angiography. AJNR Am J Neuroradiol 2000;21:162–170.
6. Sumi T, Sumi M, Van Cauteren M, Kimura Y, Nakamura T. Parallel imaging technique for the external carotid artery and its branches: comparison of balanced turbo field echo, phase contrast, and time-of-flight sequences. J Magn Reson Imaging 2007;25:1028–1034.
7. Miyazaki M, Lee VS. Nonenhanced MR angiography. Radiology 2008;248:20–43.
8. Okada T, Kanao S, Ninomiya A, et al. Whole-heart coronary magnetic resonance angiography with parallel imaging: comparison of acceleration in one-dimension vs. two-dimensions. Eur J Radiol 2008;Jul 19. DOI: 10.1016/j.ejrad.2008.06.005.
9. Shimada K, Isoda H, Okada T, et al. Non-contrast-enhanced MR angiography for selective visualization of the hepatic vein and inferior vena cava with true steady-state free-precession sequence and time-spatial labeling inversion pulses: preliminary results. J Magn Reson Imaging 2009;29:474–479.
10. Koktzoglou I, Edelman RR. Fast projective carotid MR angiography using arterial spin-labeled balanced SSFP. J Magn Reson Imaging 2008;28:778–782.
11. Xu PJ, Yan FH, Wang JH, Lin J, Fan J. Utilizing generalized autocalibrating partial parallel acquisition (GRAPPA) to achieve high-resolution contrast-enhanced MR angiography of hepatic artery: initial experience in orthotopic liver transplantation candidates. Eur J Radiol 2007;61:507–512.
12. Dietrich O, Raya JG, Reeder SB, Reiser MF, Schoenberg SO. Measurement of signal-to-noise ratios in MR images: influence of multichannel coils, parallel imaging, and reconstruction filters. J Magn Reson Imaging 2007;26:375–385.
13. Lohan DG, Barkhordarian F, Saleh R, et al. MR angiography at 3 T for assessment of the external carotid artery system. AJR Am J Roentgenol 2007;189:1088–1094.
14. Marckmann P, Skov L, Rossen K, et al. Nephrogenic systemic fibrosis: suspected causative role of gadodiamide used for contrast-enhanced magnetic resonance imaging. J Am Soc Nephrol 2006; 17:2359–2362.
15. Lell M, Tomandl BF, Anders K, Baum U, Nkenke E. Computed tomography angiography versus digital subtraction angiography in vascular mapping for planning of microsurgical reconstruction of the mandible. Eur Radiol 2005;15:1514–1520.
16. Morcos SK, Thomsen HS, Webb JA. Contrast-media-induced nephrotoxicity: a consensus report. Contrast Media Safety Committee, European Society of Urogenital Radiology (ESUR). Eur Radiol 1999; 9:1602–1613.
17. Namasivayam S, Kalra MK, Torres WE, Small WC. Adverse reactions to intravenous iodinated contrast media: a primer for radiologists. Emerg Radiol 2006;12:210–215.
18. Scheffler K, Lehnhardt S. Principles and applications of balanced SSFP techniques. Eur Radiol 2003;13:2409–2418.
19. Garcia DM, Duhamel G, Alsop DC. Efficiency of inversion pulses for background suppressed arterial spin labeling. Magn Reson Med 2005;54:366–372.
20. Michaely HJ, Herrmann KA, Dietrich O, Reiser MF, Schoenberg SO. Quantitative and qualitative characterization of vascularization and hemodynamics in head and neck tumors with a 3D magnetic resonance time-resolved echo-shared angiographic technique (TREAT)—initial results. Eur Radiol 2007;17:1101–1110.

Ann Nucl Med (2009) 23:657–669
DOI 10.1007/s12149-009-0288-7

ORIGINAL ARTICLE

Significance of chronic marked hyperglycemia on FDG-PET: is it really problematic for clinical oncologic imaging?

Tadashi Hara · Tatsuya Higashi · Yuji Nakamoto · Tsuyoshi Suga · Tsuneo Saga · Takayoshi Ishimori · Koichi Ishizu · Hidekazu Kawashima · Shigeto Kawase · Keiichi Matsumoto · Kaori Togashi

Received: 3 February 2009 / Accepted: 28 June 2009 / Published online: 7 August 2009

Abstract
Objectives The purpose of this study was to evaluate the adverse effects of chronic marked hyperglycemia on clinical diagnostic performance of positron emission tomography (PET) using ^{18}F-fuorodeoxyglucose (FDG).
Methods Fifty-seven scans of 54 patients, who received FDG-PET for the diagnosis of various cancer(s), and who showed high plasma glucose level of more than 200 mg/dl at the time of administration of FDG in spite of at least 4-h fasting, were retrospectively analyzed. In the clinical follow-up, this high plasma glucose was confirmed as chronic hyperglycemia derived from uncontrolled diabetes ($n = 32$) and untreated diabetes ($n = 25$). Based on the final diagnosis of malignancy obtained by histopathology or clinical follow-up for at least 6 months, the diagnostic performance of visual PET analysis was evaluated.
Results Excluding nine scans of nine patients without sufficient follow-up, final diagnosis was obtained in 48 scans of 45 patients. In 36 scans of 36 patients, at least one malignant lesion was finally confirmed, and true-positive and false-negative results were obtained in 30 and six cases, respectively. Six cases showed false-negative results due to low FDG-avid pathological characteristics (hepatocellular carcinoma, etc.), chemotherapeutic effect or small tumor size. Overall, the patient-based sensitivity, specificity, positive predictive value, negative predictive value and diagnostic accuracy were 83, 83, 94, 63 and 83%, respectively. In lesion-based diagnosis, 56 of 75 lesions (74%) were depicted by PET, while 19 lesions were negative on PET, also due to low FDG-avid characteristics or small size (less than 15 mm).
Conclusions At the time of chronic hyperglycemia (not acute hyperglycemia), the adverse effect caused by high plasma glucose level was minimum. The FDG uptake of the tumor maintained a sufficiently high level for visual clinical diagnosis in most cases, except in the cases of low FDG-avid tumors or small lesions (15 mm in size).

Keywords FDG-PET · Hyperglycemia · Diabetes · False negative · Tumor

T. Hara · T. Higashi · Y. Nakamoto · T. Suga · T. Ishimori · K. Ishizu · H. Kawashima · S. Kawase · K. Togashi
Department of Diagnostic Imaging and Nuclear Medicine, Kyoto University Graduate School of Medicine, Kyoto, Japan

T. Higashi (✉)
Shiga Medical Center Research Institute,
5-4-30 Moriyama, Moriyama, Shiga 524-8524, Japan
e-mail: higashi@shigamed.jp

T. Saga
Department of Diagnostic Imaging Molecular Imaging Center, National Institute of Radiological Sciences, Chiba, Japan

T. Ishimori
Department of Radiology, Kurashiki Central Hospital, Okayama, Japan

K. Matsumoto
Kyoto College of Medical Science, Kyoto, Japan

Introduction

Positron emission tomography (PET) using ^{18}F-fluoro-2-deoxy-D-glucose (FDG) has been widely used as a functional imaging tool in oncology [1]. It is known that the accumulation of FDG can be influenced by plasma glucose level on injection of FDG, because FDG is a radiolabeled glucose analog. There have been many reports mentioning the effects of hyperglycemia on FDG uptake. In vitro

studies indicated that accumulation of FDG in cancer cells declined with the increase of glucose level in the medium [2]. Torizuka et al., however, reported in their in vitro study that adenocarcinoma cells did not significantly change FDG uptake in the case of chronic hyperglycemia, while acute hyperglycemia markedly reduced FDG uptake [3]. In addition, Zhao et al. reported in their animal model that insulin loading decreased the FDG uptake into tumors, while glucose loading did not [4]. In a human study, hyperglycemia may considerably decrease FDG uptake in tumors, impair image quality and may also adversely affect the diagnostic accuracy [5, 6]. It is reported that negative PET results should be interpreted with caution in patients with hyperglycemia, who had been suspected of having pancreatic cancer [7]. It is also recommended to reschedule PET scan when the plasma glucose level is greater than 150–200 mg/dl on injection of FDG [8]. However, most of these reports with human cases focus on acute hyperglycemia and not on chronic hyperglycemia.

Acute hyperglycemia caused by meal intake can be avoided, while we have to consider the clinical application of FDG-PET scan for patients with chronic hyperglycemia, despite their prior fasting, due to diabetes. In such cases, it is not always easy to reschedule a PET scan in clinical practice. Especially, patients with pancreatic cancer have accompanying uncontrollable diabetes, and it may be preferable to perform a PET scan in spite of their hyperglycemia, rather than wait until their hyperglycemia is diminished, resulting in possible delay of treatment. For this reason, it is important to assess how much and how often chronic hyperglycemia, with a plasma glucose level of greater than 200 mg/dl, can affect the actual diagnostic accuracy in a clinical oncologic situation.

The purpose of this study was to investigate the influence of chronic hyperglycemia caused by diabetes in the diagnostic performance of FDG-PET in a clinical setting.

Patients and methods

Patients and plasma glucose evaluation

Between January 2001 and December 2005, 3459 patients underwent 4655 FDG-PET scans in our institute for suspected or known malignant disease. In our institute, patients were instructed to fast for more than 4 h before FDG injection, until the end of PET scanning. Patients who had just had a meal and patients with acute hyperglycemia caused by insufficient fasting were excluded from this investigation. Among the fasting patients, there were 71 scans of 68 patients, who showed high plasma glucose level greater than 200 mg/dl at the time of administration of FDG. Among them, 14 patients with hyperglycemia caused by unknown reasons were excluded because confirmation of diabetes was not sufficient in clinical follow-up. Finally, there were 57 scans of 54 patients (1.2%) (male:female = 38:16, mean age: 64.8 ± 9.0, ranging from 42 to 79 years old) who showed chronic hyperglycemia (greater than 200 mg/dl) at the time of administration of FDG (mean glucose level:255.5 ± 69.3, ranging from 201 to 666 mg/dl) in spite of prior fast for at least 4 h. The reasons for chronic hyperglycemia were confirmed in the clinical follow-up as follows: poorly controlled diabetes ($n = 32$) and untreated diabetes ($n = 25$). At the time of administration of FDG, 2 ml of the patient's blood was drawn via the cubitus vein and the drawn blood was collected in a plastic tube containing sodium fluoride, heparin and EDTA (ethylenediaminetetraacetic acid)-Na_2, immediately. The sample was centrifuged for 3 min at the speed of 3,000/min. The plasma sample was analyzed by GOD (glucose oxidase)-electro-enzymatic assay using automated analyzer, GA1160 (ARKRAY, Kyoto, Japan).

PET scanning

Fluorine-18 was synthesized by the nucleophilic substitution method [9] with an ^{18}F-FDG-synthesizing instrument (F-100, Sumitomo Heavy Industries, Tokyo, Japan) and a cyclotron (CYPRIS-325R, Sumitomo Heavy Industries, Tokyo, Japan). After 4-h of fasting, patients received an intravenous injection of approximately 370 MBq (10 mCi) of FDG, and PET was performed using a whole-body PET scanner (GE advance, GE healthcare, Milwaukee, WI). The scanner had 18 rings, which provided 35 tomographic sections at 4.25-mm intervals. Image reconstruction with segmented attenuation correction was performed by ordered subsets expectation maximization algorithm. The intrinsic transaxial resolution of the PET machine was measured as 3.8 m full width at half maximum (FWHM) at the center of cross section, and 7.3 mm FWHM at a radius of 20 cm (radial) from the center of cross section. The effective resolution after reconstruction was measured as 4.0 mm FWHM at the center of cross section, and 6.6 mm at a radius of 20 cm from the center of cross section.

Interpretations and analyses

PET images were interpreted visually by at least two experienced nuclear medicine physicians, using corresponding CT and MRI images (performed within 1 week before or after the date of FDG-PET study), which permitted accurate identification of the tumor relative to anatomic landmarks. CT examinations were performed with the use of Hi-Speed Advantage (GE Medical Systems; Milwaukee, WI) or CT-W2000 or CT-W3000 (Hitachi Medico; Tokyo, Japan) scanners. Pre-contrast, early and delayed post-contrast

images were obtained in all patients with abdominal lesions, and pre-contrast and post-contrast images were obtained in all patients with neck lesions, while contrast images were not obtained for the patients with chest lesions. MR imaging using T1 and T2-weighted fast spin-echo (SE) imaging was performed on a 1.5-T superconducting unit; Magnetom Symphony (Siemens, Erlangen, Germany) or Sigma Horizon (General Electric Medical System, Milwaukee, WI) with a body phased array coil for the patients with abdominal lesions, and with a neck phased array coil for the patients with neck lesions. However, MR imaging was not performed in patients with chest lesions. The patient-based diagnostic accuracy was calculated, according to final diagnoses determined by histopathology ($n = 20$) or clinical follow-up for at least 6 months ($n = 28$). Also, the frequency of false-negative findings was evaluated. In addition, FDG accumulation in malignant lesions, brain (cerebellum), liver (right lobe) and muscle (gluteal muscle) was also analyzed semi-quantitatively by calculating the standardized uptake value (SUV) in the regions of interest (ROIs) with the size of 5×5 mm^2 placed over the areas.

$$\text{Standardized uptake value (SUV)} = \frac{\text{PET count} \times \text{calibration factor (mCi/g)}}{\text{injection dose (mCi)/body weight (g)}}$$

The ROI was placed in tumor areas that showed the highest FDG activity, and the maximum SUV (SUVmax) in the ROIs of the lesion was defined as the SUV of the tumor.

If patients had more than six malignant lesions, only five lesions were analyzed. Physiological FDG uptake in the brain, liver and muscle (hip muscle was used as reference) was also examined in each case by calculating the averaged SUV of the five ROIs in five different slices of each organ. For the comparison of normal FDG uptake in brain, liver and muscle, randomly chosen 50 normoglycemic patients who received FDG-PET study for the evaluation of cancer in the body, not brain or liver tumor, between January 2001 and December 2005 were analyzed (mean glucose level: 88.5 ± 12.4).

Results

Nine scans of nine patients without sufficient oncologic follow-up were excluded from the analysis, because of unconfirmed final cancer status. Since three patients had a PET scan twice, we analyzed 48 scans in 45 patients. In these three patients, two scans were performed with more than 1-year interval between two scans. Therefore, we defined these two scans as two different cases. At least one malignant site was finally diagnosed in 36 of 48 cases (Table 1), while the final diagnoses were negative (no malignant lesion) in 12 of 48 cases (Table 2).

In 36 cases with malignant lesion, 30 cases showed true-positive primary lesion by PET diagnosis even under hyperglycemia, while six cases showed false negative. In 30 cases with true-positive results, 19 cases showed multiple foci. Among these 19 cases, two cases had numerous lung metastases and one had multiple bone metastases, but many lesions were clearly depicted by PET (Fig. 1). Among the 12 cases who had no malignant lesion, 10 cases were accurately diagnosed as true-negative and two cases were interpreted as positive with the final diagnosis of false positive (Table 2). These false-positive findings were considered to be due to the physiological uptake in the colon and biloma. Six false-negative cases for primary lesion were small-sized bile duct cancer ($n = 1$), hepatocellular carcinoma (well-differentiated: $n = 2$, poorly differentiated with small size: $n = 1$; $n = 3$), lung cancer (adenocarcinoma, post-radiation, $n = 1$), and pancreatic cancer (scirrhous type, $n = 1$) (Fig. 2) (Table 3). In 11 cases of lung cancer in this study, tumor detectability was 10/11 cases (91%) with only one false-negative case. In 11 cases of pancreatic cancer, tumor detectability was 10/11 cases (91%) with only one false-negative case (Fig. 2). On the other hand, there was only one case of bile duct cancer and four cases of hepatocellular carcinoma (tumor detectability was 0 and 25%, respectively). Overall, the patient-based sensitivity, specificity, positive predictive value, negative predictive value and diagnostic accuracy were 83, 83, 94, 63 and 83%, respectively.

In lesion-based diagnosis, 56 of 75 lesions (74%) were depicted by PET, while 19 lesions were negative on PET mainly due to small size (less than 15 mm) (Table 3). Thirteen false-negative lesions for additional lesions were three bone metastases (two osteoblastic lesions, one post-radiotherapeutic lesion), one lung lesion with ground-glass opacity (well-differentiated adenocarcinoma) and 9 small lesions (less than 15 mm in size).

In the quantitative analysis of FDG uptake in cancer tissue, there was no apparent decrease in the SUVmax of tumor, despite hyperglycemia (Fig. 3a). SUVmax of tumor did not show a tendency to continuous decrease with the increase of plasma glucose level (n.s.). Even in the false-negative cases, FDG uptake was kept relatively high (more than 2.0) for several lesions (Table 3). With regard to the physiological uptake, FDG uptake in the brain showed a significant constant decrease with the increase in plasma glucose level (R^2 0.3888) and tended to be lower in the present study (4.5 ± 1.0), as compared to that (11.8 ± 2.6) in the randomly chosen 50 patients with normoglycemia (mean glucose level:88.5 ± 12.4) (Fig. 3b). However, uptake in the liver (3.3 ± 0.5) and muscle (1.4 ± 0.4) was not influenced significantly by chronic hyperglycemia, as compared to those (2.9 ± 0.8,

Table 1 Patients' profile in malignant cases

Case no.	Age	Gender	Plasma glucose level (mg/dl)	Final diagnosis	Result	Method of diagnosis	Lesion1			Lesion2			Lesion3		
							Primary or metastatic site	SUVmax	PET results	Metastatic site	SUVmax	PET results	Metastatic site	SUVmax	PET results
1	59	F	331	Adrenal cancer, lung mets	TP	op	Adrenal	3.8	TP	Lung	na	FN(3)	–		
2	77	F	223	Bile duct cancer	FN	op	Liver	3.8	FN(na)	–			–		
3	52	F	282	Breast cancer[b], bone mets	TP	f/u	Bone1	3.3	TP	Bone2	na	FN(30[d])	–		
4	67	F	215	Breast cancer[b], bone mets	TP	op	Bone1	5.1	TP	Bone2	3.2	TP	Bone3	2.9	TP
5	58	M	235	Buccal mucosa cancer, LN mets	TP	op	Buccal mucosa	9.4	TP	LN	6.1	TP	–		
6	59	M	236	Colorectal cancer[b], liver and LN mets	TP	f/u	Liver1	5.6	TP	Liver2	4.6	TP	LN	6.2	TP
7	64	M	291	Colorectal cancer[b], lung mets	TP	f/u	Lung1	6.5	TP	Lung2	4.1	TP	Lung3	3.8	TP
8	61	M	279	Gastric cancer[b], liver mets	TP	f/u	Liver	4.2	TP	–			–		
9	54	M	203	Gastric cancer[b], peritonitis carcinomatosa	TP	f/u	Peritoneum	3.2	TP	–			–		
10	76	M	206	Gastric cancer, liver mets	TP	f/u	Liver	5.2	TP	Stomach	4.6	TP	LN	3.5	TP
11[a]	56	M	212	Hepatocellular carcinoma	FN	op	Liver	2.9	FN(25)	–			–		
12	51	M	236	Hepatocellular carcinoma	FN	op	Liver1	1.8	FN(14)	–			–		
13	56	F	245	Hepatocellular carcinoma, liver mets	FN	op	Liver1	3.4	FN(22)	Liver2	2.9	FN(15)	Liver2	na	FN(13)
14	63	F	303	Hepatocellular carcinoma[b], LN mets	TP	op	LN	4.8	TP[c]	–			–		
15	71	M	205	Lung cancer	TP	op	Lung	11.6	TP	–			–		
16	70	M	224	Lung cancer	TP	f/u	Lung	3.5	TP	–			–		
17	74	M	242	Lung cancer	TP	f/u	Lung	5.0	TP	–			–		
18	72	M	264	Lung cancer	FN	f/u	Lung	2.1	FN(25[c])	LN	na	FN(na[c])	–		
19	75	F	204	Lung cancer[b], bone mets	TP	f/u	Bone	2.3	TP[d]	–			–		
20	67	M	249	Lung cancer[b], lung and liver mets	TP	f/u	Lung1	12.3	TP	Lung2	3.3	TP	Liver	5.4	TP
21	51	M	237	Lung cancer, LN and bone mets	TP	bx	Lung	4.8	TP	LN1	6.3	TP	LN2	5.6	TP
22	64	M	237	Lung cancer, LN mets, with GGO	TP	f/u	Lung1	5.0	TP	LN	3.4	TP	Lung (GGO)	na	FN(17)
23	71	M	240	Lung cancer, LN mets	TP	f/u	Lung	2.6	TP	LN	4.0	TP	–		
24	76	M	203	Lung cancer, LN mets	TP	bx	Lung1	8.5	TP	Lung2	5.9	TP	LN	3.4	TP
25	66	M	375	Lung cancer, LN mets	TP	bx	Lung	5.7	TP	LN1	4.7	TP	LN2	3.5	TP
26	67	M	220	Pancreas cancer	TP	op	Pancreas	3.7	TP	–			–		
27[a]	71	M	231	Pancreas cancer	TP	op	Pancreas	3.4	TP	–			–		
28	42	M	301	Pancreas cancer	TP	op	Pancreas	2.3	TP	–			–		
29	77	M	205	Pancreas cancer	TP	op	Pancreas	4.4	TP	LN	na	FN(7)	–		

Table 1 continued

Case no.	Age	Gender	Plasma glucose level (mg/dl)	Final diagnosis	Result	Method of diagnosis	Lesion1			Lesion2			Lesion3		
							Primary or metastatic site	SUVmax	PET results	Metastatic site	SUVmax	PET results	Metastatic site	SUVmax	PET results
30	69	M	212	Pancreas cancer	FN	op	Pancreas	2.4	FN(35)	–			–		
31	74	M	203	Pancreas cancer (IPMC)	TP	op	Pancreas	5.9	TP	–			–		
32	72	M	204	Pancreas cancer, liver mets	TP	f/u	Pancreas	5.4	TP	Liver	3.9	FN(9)	–		
33	70	M	271	Pancreas cancer, liver mets	TP	op	Pancreas	7.8	TP	Liver	na	FN(na)	–		
34	74	M	208	Pancreas cancer, LNs mets	TP	f/u	Pancreas	5.2	TP	LN	2.5	FN(5)	–		
35	65	M	374	Pancreas cancer, LNs mets	TP	f/u	Pancreas	3.0	TP	LN	na	FN(11)	–		
36[a]	67	F	253	Pancreas cancer[d], lung mets	TP	f/u	Lung1	2.7	TP	Lung2	2.4	TP	Lung3	2.3	TP

Case no.	Age	Gender	Plasma glucose level (mg/dl)	Final diagnosis	Result	Method of diagnosis	Lesion4			Lesion5		
							Metastatic site	SUVmax	PET results	Metastatic site	SUVmax	PET results
1	59	F	331	Adrenal cancer, lung mets	TP	op	–			–		
2	77	F	223	Bile duct cancer	FN	op	–			–		
3	52	F	282	Breast cancer[b], bone mets	TP	f/u	–			–		
4	67	F	215	Breast cancer[b], bone mets	TP	op	Bone4	2.7	TP	–		
5	58	M	235	Buccal mucosa cancer, LN mets	TP	op	–			–		
6	59	M	236	Colorectal cancer[b], liver and LN mets	TP	f/u	–			–		
7	64	M	291	Colorectal cancer[b], lung mets	TP	f/u	Lung4	3.8	TP	Lung5	3.7	TP
8	61	M	279	Gastric cancer[b], liver mets	TP	f/u	–			–		
9	54	M	203	Gastric cancer[b], peritonitis carcinomatosa	TP	f/u	–			–		
10	76	M	206	Gastric cancer, liver mets	TP	f/u	–			–		
11[a]	56	M	212	Hepatocellular carcinoma	FN	op	–			–		
12	51	M	236	Hepatocellular carcinoma	FN	op	–			–		
13	56	F	245	Hepatocellular carcinoma, liver mets	FN	op	–			–		
14	63	F	303	Hepatocellular carcinoma[b], LN mets	TP	op	–			–		
15	71	M	205	Lung cancer	TP	op	–			–		
16	70	M	224	Lung cancer	TP	f/u	–			–		
17	74	M	242	Lung cancer	TP	f/u	–			–		
18	72	M	264	Lung cancer	FN	f/u	–			–		
19	75	F	204	Lung cancer[b], bone mets	TP	f/u	–			–		
20	67	M	249	Lung cancer[b], lung and liver mets	TP	f/u	–			–		
21	51	M	237	Lung cancer, LN and bone mets	TP	bx	Bone1	2.7	FN(40)	Bone2	na	FN(30)
22	64	M	237	Lung cancer, LN mets, with GGO	TP	f/u	–			–		

Table 1 continued

Case no.	Age	Gender	Plasma glucose level (mg/dl)	Final diagnosis	Result	Method of diagnosis	Lesion4			Lesion5		
							Metastatic site	SUVmax	PET results	Metastatic site	SUVmax	PET results
23	71	M	240	Lung cancer, LN mets	TP	f/u	–			–		
24	76	M	203	Lung cancer, LN mets	TP	bx	–			–		
25	66	M	375	Lung cancer, LN mets	TP	bx	–			–		
26	67	M	220	Pancreas cancer	TP	op	–			–		
27[a]	71	M	231	Pancreas cancer	TP	op	–			–		
28	42	M	301	Pancreas cancer	TP	op	–			–		
29	77	M	205	Pancreas cancer	TP	op	–			–		
30	69	M	212	Pancreas cancer	FN	op	–			–		
31	74	M	203	Pancreas cancer (IPMC)	TP	op	–			–		
32	72	M	204	Pancreas cancer, liver mets	TP	f/u	–			–		
33	70	M	271	Pancreas cancer, liver mets	TP	op	–			–		
34	74	M	208	Pancreas cancer, LNs mets	TP	f/u	–			–		
35	65	M	374	Pancreas cancer, LNs mets	TP	f/u	–			–		
36[a]	67	F	253	Pancreas cancer[d], lung mets	TP	f/u	Lung4	2.3	TP	Lung5	2.2	TP

TP true positive, *FN* false negative, *LN* lymph node, *mets* metastasis, *IPMC* intraductal papillary mucinous carcinoma, *op* operation, *bx* biopsy, *f/u* clinical follow-up, *na* not available, *GGO* ground-glass opacity

Lesion size in parentheses (mm). Size was not measured in some lesions because imaging findings did not depict the lesions and there was no information on pathological reports

[a] Same patients shown as different cases in Table 2 (No. 36 = No. 39, No. 11 = No. 42, No. 27 = No. 47)

[b] Post-operative state

[c] Post-chemotherapy (within 1 month)

[d] Post-radiation therapy (within 1 month)